

The gas kinematics in Mrk 533 nucleus and circumnuclear region: a gaseous outflow

A. A. Smirnova^{1*}, N. Gavrilović^{2,3}, A. V. Moiseev¹, L. Č. Popović², V. L. Afanasiev¹, P. Jovanović², M. Dačić²

¹*Special Astrophysical Observatory, Nizhnij Arkhyz 369169, Russia*

²*Astronomical Observatory, Volgina 7, Belgrade, 11160, Serbia*

³*Université de Lyon, Lyon, F-69000, France ; Université Lyon 1, Villeurbanne, F-69622, France Centre de Recherche Astronomique de Lyon, Observatoire de Lyon, 9 avenue Charles André, Saint-Genis Laval cedex, F-69561, France ; CNRS, UMR 5574 ; Ecole Normale Supérieure de Lyon, Lyon, France*

17 July 2017

ABSTRACT

We present an analysis of 3D spectra of Mrk 533, observed with the integral-field spectrograph MPFS and using the Fabry Perot Interferometer (FPI) of the SAO RAS 6-m telescope. We found emissions of gas from the active Sy 2 nucleus in the centre and also from the HII regions in a spiral structure and a circumnuclear region. The gas kinematics shows regular non-circular motions in the wide range of galactocentric distances from 500 pc up to 15 kpc. The maps of inward and outward radial motions of the ionized gas was constructed. We found that the narrow line region (NLR) is composed of at least two (probably three) kinematically separated regions. We detect a stratification in the NLR of Mrk 533 with the outflow velocity ranging from 20-50 km s⁻¹ to 600-700 km s⁻¹, respectively, on the radial distances of ~ 2.5 and ~ 1.5 kpc. The maximal outflow velocity comes from the nucleus and corresponds to the position of the observed radio structure, which is assumed to be created in an approaching jet. We suggest that these ionized gas outflows are triggered by the radio jet intrusion in an ambient medium.

Key words: galaxies: kinematics and dynamics – galaxies: Seyfert – galaxies: jets – galaxies: individual: Mrk 533.

1 INTRODUCTION

Theoretical studies have shown that the interactions of galaxies can bring gas from the disc towards the nuclear regions, and that they can also produce a burst of star formation (Perez et al. 2006). Therefore, the detailed investigation of the emission of gas kinematics in nearby Seyfert galaxies is very important. The panoramic (3D) spectroscopy is a powerful tool for this goal. Here we present a spectroscopic study of Mrk 533, an interacting Sy 2 galaxy. Mrk 533 (also denoted as NGC 7674, Arp 182, UGC 12608, H96a) is the brightest member of the Hickson 96 compact group of galaxies (Hickson 1982). It is the only spiral (Sbc pec) galaxy among other tidally interacting galaxies in the group (Verdes-Montenegro et al. 1997). The kinematics of Mrk 533 was observed twice with scanning Fabry-Perot systems (Afanasiev & Kostiuik 1996; Amram et al. 2003) and once using the long slit-spectra technique (Verdes-Montenegro et al. 1997).

Afanasiev & Kostiuik (1996) mapped the velocity field in the H α line observed with the 6-m telescope using FPI. The spectral resolution was $\delta\lambda \approx 1.0 \text{ \AA}$ and the free (interfringe) spectral range was $\Delta\lambda \approx 13 \text{ \AA}$. They also used an integral-field data and reported a complex structure of emission lines in the central region within $r < 5$ arcsec, where the H α has a broad and narrow component. Moreover, the narrow component could be also divided into two Gaussians, where one of them corresponds to the normal rotation and second seems to be connected with the nuclear radio structure. Afanasiev & Kostiuik (1996) found non-circular motions that are probably caused by the circumnuclear bar. Amram et al. (2003) also observed Mrk 533 and its environment with 3.6-m ESO Telescope using the FPI system ($\delta\lambda \approx 0.7 \text{ \AA}$ and $\Delta\lambda \approx 8.5 \text{ \AA}$). They found a significant disagreement in shape of radial velocity distribution between receding and approaching sides of the galactic discs at distances $r > 20$ arcsec. A possible shift of the rotation centre around 2 arcsec with respect to the optical centre was also noted. Both features are probably caused by interactions with companions, especially with HCG96c.

* E-mail: alexiya@sao.ru

Mrk 533 is a Sy 2 galaxy where the broad H α and H β lines are observed in polarized flux (Miller & Goodrich 1990), indicating the presence of a hidden Broad Line Region (Tran 1995). In addition, the Narrow Line Region of Mrk 533 is extended, as shown in the [OIII] $\lambda\lambda 4959, 5007$ image observed with HST (Schmitt et al. 2003). Unger et al. (1988) found that radio maps reveal the presence of a triple radio source with a total angular extent of about 0.7 arcsec. This provides evidence that the radio emission is powered by ejection. In the plane of the sky, the ejection axis is found to be roughly perpendicular to the galactic rotation axis (Unger et al. 1988). Recently, VLBI continuum and HI absorption observations of the central part with 100 mas resolution, showed six continuum structures extending over 1.4 arcsec (742 pc), with a total flux density of 138 mJy (Momjian et al. 2003). Momjian et al. (2003) also suggested that the overall S-shaped radio pattern could be the result of an interstellar medium diverting the out-coming jets from the central AGN. In the same time, they could not rule out the possibility of a black hole merger that could result in a similar structural pattern.

The galaxy has noticeable blue-shifted wings on almost all of the emission lines (except [SII] $\lambda\lambda 6716, 6730\text{\AA}$) as originally suggested by Afanasiev et al. (1980) and later confirmed by other authors (e.g. Shuder & Osterbrock (1981), Laurikainen & Moles (1988), De Robertis & Shaw (1990), Veilleux (1991), etc.). Moreover, the observed UV doublet O VI $\lambda\lambda 1032, 1038$ line profile shows a blue wing that indicates an outflow in the UV emission gas (Shastri et al. 2006). Also, the absorption lines at -300 km s^{-1} and -800 km s^{-1} have been observed in the O VI doublet (Shastri et al. 2006). The absorption in the O VI and a blue asymmetry in the optical lines might be caused by an accelerated wind from the central source.

Here we present an analysis of Mrk 533 spectra observed with 6-m telescope of the SAO RAS using the integral-field spectrograph MPFS and Fabry-Perot Interferometer (FPI). The aims of the paper are: (i) to investigate the emission line structures of Mrk 533, focusing on the central part in order to map gaseous outflows indicated in the previous radio and UV observations; (ii) to study the gas kinematics in the circumnuclear region. Also, here we will discuss the kinematics of a gaseous disc as a whole which has a non-circular component of motion in order to find the link between the host galaxy and central part kinematics.

In this paper we adopt the value of 116 Mpc given by Momjian et al. (2003), to be the Mrk 533 distance, using the scale $1\text{ arcsec}=563\text{ pc}$.

The paper is structured as follows: In Section 2 we present our observations, in Section 3 we analyze the gas kinematics in Mrk 533, in Section 4 we investigate in more detail the complex NLR in this galaxy, in Section 5 we discuss the possible link between the radio jet and optical one, and finally in Section 6 we give our conclusions.

2 OBSERVATIONS AND DATA REDUCTION

The panoramic (or 3D) spectroscopy provides spectra of extended object simultaneously for each spatial element in a

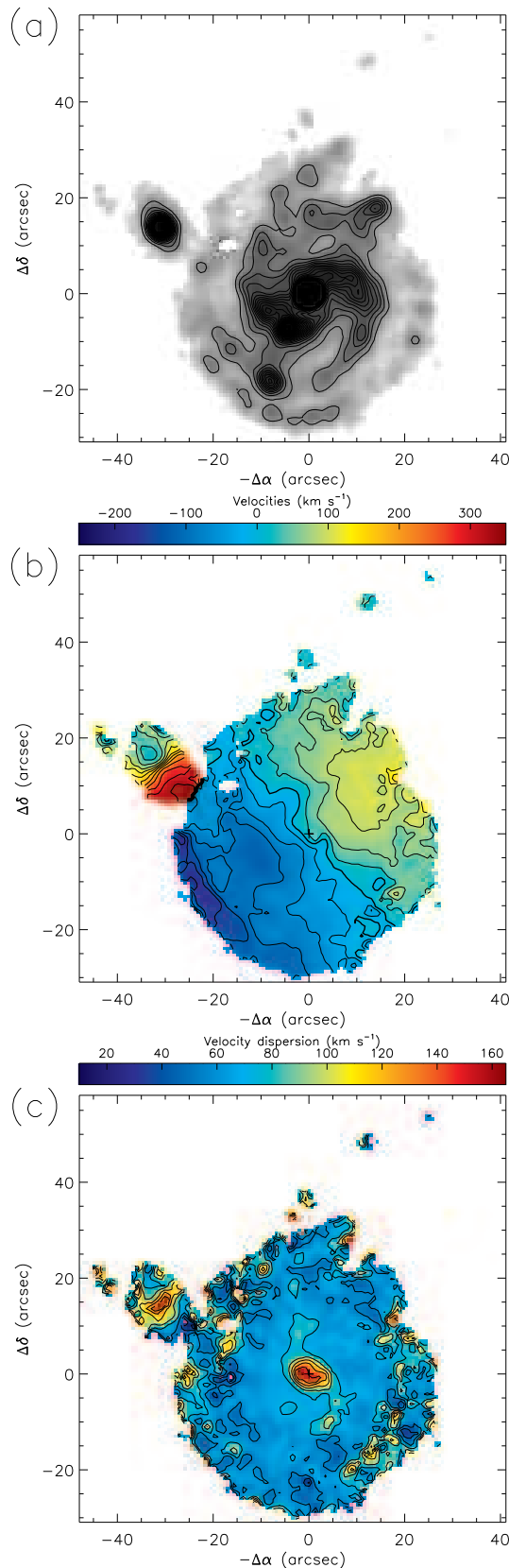


Figure 1. Large-scale emission-line intensity distribution in log-scale (a), ionized-gas line-of-sight velocity field minus the systemic velocity (b) and velocity dispersion (c) for Mrk 533 obtained from FPI data for the H α line. The cross corresponds to the continuum centre. The thick contour on (b) marks the zero velocity.

Table 1. The spectroscopic observations of Mrk 533.

Date	T_{exp} (sec)	Sp. Range (Å)	Sp. Res. (Å)	Seeing (arcsec)	Instrument
1998 Aug. 30	24×180	H α	3.0	1.5	FPI
2002 Aug. 13	3600	4500 - 7100	7.5	1.5	MPFS
2005 Sep. 28	6000	4350 - 5900	4.2	1.3	MPFS

two-dimensional field of view (FOV). We used two different types of 3D spectrographs: the integral-field spectrograph MPFS and scanning FPI. The first device provides a detailed spectral information in the spectral range about several thousand Å what is important for the goals of the spectrophotometry and for analyzing the broad line profiles. However, the FOV of MPFS is small (less than 16 arcsec), it can cover only a region around the active nucleus of Mrk 533. In contrast, the scanning FPI had a very large FOV (a few arcmin) with a very narrow spectral region containing only a spectral line. Using this device we are able to investigate the long-scale kinematics of the ionized gas in the whole stellar disc of Mrk 533, but only in the narrow component of the H α emission line.

2.1 Integral-Field Spectrograph MPFS

Mrk 533 was observed in August 2002 and September 2005 using the MultiPupil Fiber Spectrograph (MPFS), with the integral-field unit mounted at the primary focus of the 6-m telescope (Afanasiev, Dodonov & Moiseev 2001). The MPFS takes simultaneous spectra of 240 spatial elements (constructed in the shape of square lenses) that form on the sky an array of 16×15 elements (in 2002), or of 256 spatial elements (16×16 in 2005). The angular size was 1 arcsec per element in 2002, and 0.75 arcsec per element in 2005. The detectors were a CCD TK1024 (1024×1024 px) in 2002 and EEV42-40 (2048×2048 px) in 2005. A description of the MPFS is available at SAO RAS web page <http://www.sao.ru/hq/lsvfo/devices.html>.

During the first run, in August 2002, for spectrophotometry purposes, the galaxy was observed at a low resolution, while during the second run it was subject to a kinematics investigation of the NLR, and was observed at a higher resolution. The log of MPFS observations is given in Table 1.

The data were reduced using the software developed at the SAO RAS by V.L. Afanasiev and A.V. Moiseev and running in the IDL environment. The primary reduction included bias subtraction, flat-fielding, cosmic-ray hits removal, extraction of individual spectra from the CCD frames, and their wavelength calibration using a spectrum of a He-Ne-Ar lamp. Subsequently, we subtracted the night-sky spectrum from the galaxy. The spectra of the spectrophotometry standard stars were used to convert counts into absolute fluxes.

2.2 Scanning Fabry-Perot Interferometer

The galaxy was observed in August 1998 with the scanning FPI. The Queensgate interferometer ET-50 was used in the 235th interference order (for the H α line). The free spectral range between neighboring orders (interfringe) was

about 30 \AA . For monochromatization a narrow-band filter ($FWHM = 31 \text{ \AA}$) centred on the spectral region containing the redshifted H α was used. During the observations we successively took 24 interferometric images of the object with different gaps between the FPI plates. The spectral channels were of $\delta\lambda \approx 1.2 \text{ \AA}$ width, ($\sim 56 \text{ km s}^{-1}$), the spectral resolution (the width of instrumental contours) was $FWHM \approx 3.0 \text{ \AA}$ ($\sim 140 \text{ km s}^{-1}$). The detector was a CCD TK1024 (1024×1024 pixels) operated by 2×2 binning for reading-out time economy. Therefore each spectral channel had a 512×512 pixels format with the scale 0.68 arcsec per pixel. The log of the FPI observations is presented in Table 1.

To reduce the interferometric observations we used a special software (Moiseev 2002), running in the IDL environment. After the primary reduction (bias, flat-field, cosmic hits), we removed the night-sky spectrum, converted the data to a wavelength scale, and prepared them as a ‘data cube’. The spatial resolution after data reduction smoothing was about 2.5 arcsec. The velocity fields of the ionized gas, and images in the H α emission line were mapped using the Gaussian fitting of the emission line profiles. Moreover, we created an image of the galaxy in the continuum close to the emission line.

3 THE KINEMATICS OF MRK 533

3.1 Analysis of FPI observations

Both previous observations were performed using the FPI (Afanasiev & Kostiuik 1996; Amram et al. 2003) with a high spectral resolution $\delta\lambda = 0.7 - 1.0 \text{ \AA}$ but within a small spectral range ($\Delta\lambda = 8.5 - 13 \text{ \AA}$). We performed new observations with the 6-m telescope with a relatively low spectral resolution ($\delta\lambda \approx 3.0 \text{ \AA}$), but with a larger $\Delta\lambda \approx 30 \text{ \AA}$. It is important for the study of the emission line profile in the nucleus, where FWHM of lines reaches $8 - 10 \text{ \AA}$. Unfortunately, this spectral range is insufficient for a detailed analysis of emission line profiles, with FWHM larger than 30 \AA (see Section 4). Therefore, with FPI we have considered only kinematics of the narrow component of the H α . For investigation, the broad component and the blue-wing asymmetry of the [OIII] lines we have used MPFS data only.

The H α monochromatic image, obtained with FPI, is shown in Fig. 1a. As one can see in Fig. 1a, besides the strong central part in the H α , there are structures (which follow the bar and spiral arms) which show a significant H α emission. The ionized gas velocity field and velocity dispersion map (corrected on the instrumental contour) are shown in Figs 1b,c.

As can be seen in Fig. 1b, the rotation axis is SW-NE oriented. It is interesting to note that in the velocity

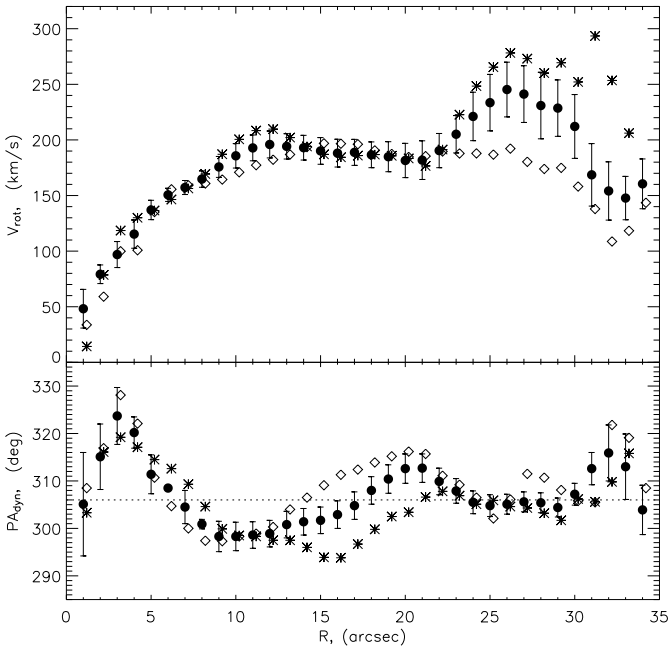


Figure 2. Results of the tilted-ring analysis of the H α velocity field: radial variations of the rotation velocities (*top*) and position angles (*bottom*). Full circles, stars and open diamonds denote the value calculated on the whole disc, SE (approaching) and NW (receding) sides respectively. Dotted line corresponds to $PA_0 = 306^\circ$ adopted in this paper (see for details Section 3.2).

map two features with approaching velocities (with respect to the systematic one) are present. These features will be discussed in more details in Subsection 4.4. The velocity dispersion map (Fig. 1c) shows the arms near the centre and, as expected, the maximum velocity dispersion in the central part.

Our maps seem to be slightly deeper than the ones given by Amram et al. (2003). For instance, we detected the velocities in several emission clumps along tidal tail located at the North of the galaxy. The field-of-view contains also a nearby satellite HCG96c located to the NE from the Mrk 533. We measured the systemic velocity of this companion, and obtained 8850 km s^{-1} ($z=0.0295$). This is in good agreement with the value given by Verdes-Montenegro et al. (1997), and different around $\sim 200 \text{ km s}^{-1}$ from the results of Amram et al. (2003).

3.2 The model of pure circular rotation

The velocity field was analyzed using the so called ‘tilted-rings’ method by Begeman (1989)¹. We were looking for the parameters of the galactic gaseous disc orientation, i.e. a line of node position angle (major axis) PA_0 and the galactic plane inclination i_0 . The velocity field was fitted using a pure circular rotation model by fixing the centre position and systemic velocity. We excluded from the analysis the central region ($r < 7 \text{ arcsec}$) where strong non-circular motions are present (see Section 4) and the external points

¹ See also Moiseev, Valdés & Chavushyan (2004) and references therein for more details.

($r > 25 \text{ arcsec}$) where the velocity field is significantly asymmetrical, as already noted by Amram et al. (2003). The following values were found from a χ^2 -minimization routine of residuals between the observed and modeled velocity fields: $i_0 = (33 \pm 5)^\circ$, $PA_0 = (306 \pm 4)^\circ$. We assumed that the position of the kinematic centre corresponds to the velocity field centre symmetry. The obtained systemic velocity is $V_{sys} = 8672 \pm 3 \text{ km s}^{-1}$ ($z=0.0289$). The kinematic centre of the galaxy is shifted for 1 pixel (or 0.7 arcsec) to the South from the continuum centre. This centre offset (lopsidedness) was already mentioned by Amram et al. (2003) and Verdes-Montenegro et al. (1997), however different authors found different positions of the centre offset. The observed shift of the kinematic centre might be due to the interaction with the companion as well as with matter that has a non-circular motion caused by the bar’s gravitational potential.

The orientation parameters are in accordance with the ones measured by Verdes-Montenegro et al. (1997), $PA = 121^\circ$ (i.e. 301°), $i = 31^\circ$, while these values are significantly different to the ones reported by Amram et al. (2003), $PA = 132 \pm 5^\circ$ and $i = 50 \pm 5^\circ$.

3.3 Detailed analysis of the H α velocity field

In order to study the nature of the deviations from the normal rotations, the velocity field was divided into elliptical rings with a 1 arcsec width aligned to the accepted PA_0 and i_0 . Using the χ^2 minimization routine for deviations of the observational points from the model, we calculated, for each radius, the position angles of the major axis $PA_{dyn}(r)$ (dynamical position angle) and the mean of rotational velocity $V_{rot}(r)$. The results of the best-fitting are shown in Fig. 2, where results for approaching (asterisk in Fig. 2) and receding sides (diamonds in Fig. 2) are shown. These are calculated separately. As was noted in Amram et al. (2003) earlier, we obtained a different kinematics between these two sides.

The mean (‘in the whole disc’) rotation curve shows a very unusual shape at distances larger than $r = 20 \text{ arcsec}$. The maximum is at $r \approx 26 \text{ arcsec}$, after that the rotational velocity decreases. As it is shown in Fig. 2, this maximum in the mean rotational curve is caused by increase of the rotation velocity (after $r > 20 \text{ arcsec}$) in the approaching (SE) side of the disc, while $V_{rot}(r)$ of the receding side is slightly decreasing in this region. Also, a small $V_{rot}(r)$ peak in the approaching side can be noticed between 10 and 14 arcsec. These features cannot be caused by specific mass distribution, but rather by an interaction with other members of the Hickson group, especially at the maximum $r > 20 \text{ arcsec}$.

There are two main possibilities, both triggered by a close interaction: (i) non-circular gas motions (first of all inwards gas streaming, see Iono et al. (2004) and references therein) and/or (ii) quasi-circular gas motions with the orientation parameters which are different from the inner galactic disc ones (warped outer disc, see Binney (1992) for review).

In case (i) we can estimate the peculiar velocities via the map of residual velocities (the differences between the observed line-of-sight velocity field and the circular model, see Section 3.4). The ‘blue’ excess of the observed velocities ($-(30 - 60) \text{ km s}^{-1}$) appear near the major axis at $r > 25 \text{ arcsec}$ on both sides of the centre if we compare the observed

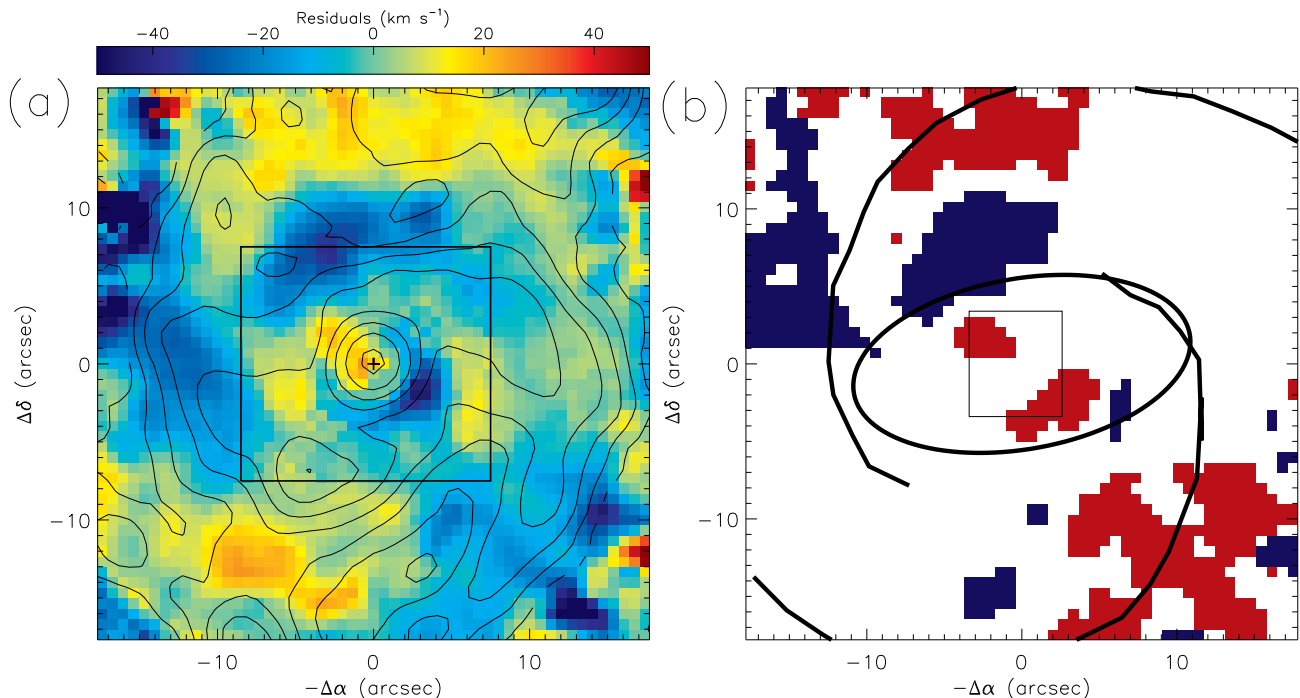


Figure 3. Ionized gas kinematics in the central region: (a) residual velocities after subtraction of the model of pure circular rotation from the observed velocity field, H α isophote are overlapped, the box corresponds to MPFS field from Fig. 10b; (b) the map of radial motions: the inflow is denoted with blue and the outflow is red. The galactic bar and spiral arms are shown. The central region mapped with MPFS (Figs. 5-9) is shown as a small box in the centre.

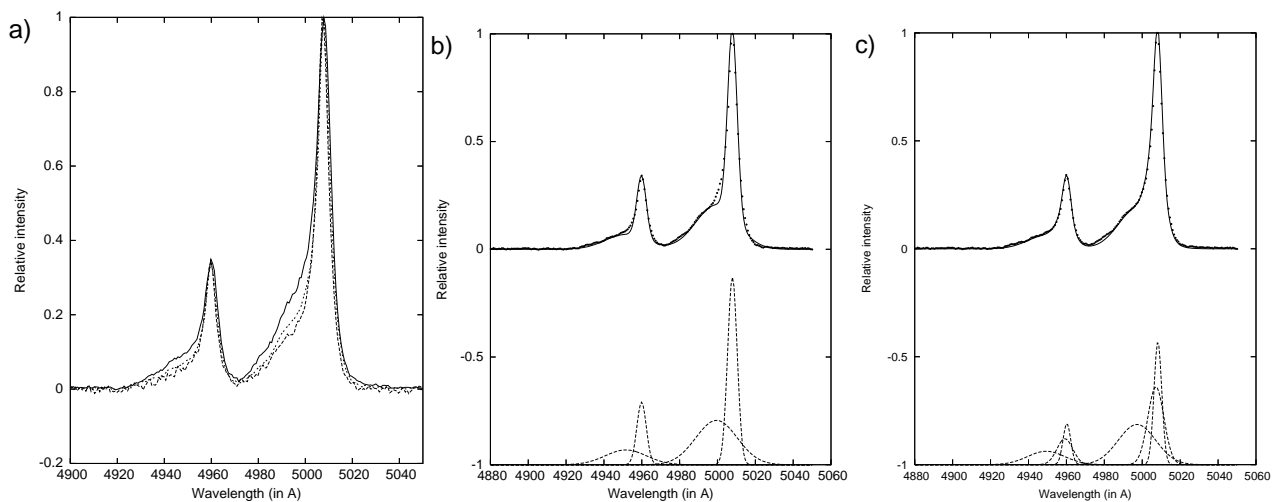


Figure 4. Difference in the blue part of the [OIII] lines across the central (nucleus) part of Mrk 533 (a). Decomposition of the [OIII] lines with two (b) and three (c) Gaussian components. Dots represent the observation and the solid line represent the best-fitting. Gaussians are shown below.

data with the model calculated for the whole disc (the full circles in Fig. 2). On the SE side of the disc the peculiar velocities located in the outer part of the spiral arm are directed towards the companion HCG96c. An asymmetric shape of this part of the spiral structure is due to the interaction with the satellites (Verdes-Montenegro et al. 1997). The line-of-sight projection of the radial motions is zero towards the major axis; using equation (1) from Section 3.4 we can obtain the residual velocities in the SE spiral arm. That correspond to the vertical velocities of up to 70 km s^{-1} or

to the azimuthal streaming in the galactic plane of $80 - 120 \text{ km s}^{-1}$ (in the direction of the rotation). These strong non-circular velocities are similar to the ones observed in the grand design spiral interaction galaxies, as e.g. in M51, with velocities $\pm(70-130) \text{ km s}^{-1}$ reported by Vogel et al. (1993).

On the other hand, the situation on the NW side of the disc is different. The residual velocities in the outer regions of the NW disc side have similar amplitude as on the SE side, but it is only in the interarm region and it has no connection with the morphological structure of the disc. At

the same time the deviations from the circular model are around zero in the NW spiral arm and in the tidal tail at the North. Moreover, if we calculate the model of rotation only for the NW side of the disc (the diamonds in Fig. 2) the peculiar velocities in the interarm region decrease significantly. Therefore, the non-circular velocities here seem to be linked to the global distinctions in the orientation parameters of the gaseous disc at a different values of r (i.e. a warped disc).

If there is a case of warped disc, one can estimate the warping angle of the disc assuming a constant rotation velocity along the radius. We found that for $r = 35$ arcsec the inclinations are $i' = (20 \pm 4)^\circ$ and $i' = (48 \pm 5)^\circ$ for SE and NW sides of the disc, respectively. Therefore, if the disc is warped between $r = 20$ arcsec and 35 arcsec is moderate, $|i' - i_0| = (13 \pm 6)^\circ$ for SE and $(15 \pm 7)^\circ$ for NW sides. As we already mentioned above, it is possible for both mechanisms to contribute to the observed kinematics: a significant non-circular motions along the SE arm and warped disc in the NW side of the galaxy.

The radial variations in PA_{dyn} around the line-of-nodes is $10 - 20^\circ$ in amplitude (see Fig. 2). It indicates non-circular gas motions. Exactly, at $r < 7$ arcsec the dynamical axis turns in the opposite side to the major axis of the near-infrared isophote of the circumnuclear bar with $PA_{photometry} \approx 280^\circ - 290^\circ$ (see Fig. 1 in Hunt et al. 1997). This type of PA_{dyn} variation corresponds to the radial streaming motion along the bar (see discussion and references in Moiseev et al. 2004). We note here that these motions should be bi-symmetrical, since measurements of PA_{dyn} show a good agreement between the SE and NW sides of the disc. Compare to the bar's region, the PA_{dyn} deviations at large distances ($r = 13 - 22$ arcsec) are significantly different at the SE and NW sides of the disc. The possible explanation to this mismatch, is an influence of the spiral arms on gaseous disc kinematics. The shape of the spiral pattern is asymmetric Verdes-Montenegro et al. (1997), hence the Northern and Southern arms cause different amplitudes (and characters) of velocity perturbations, as it is shown in Fig. 2.

3.4 The map of non-circular motions

For a precise analysis of the gas kinematics in the circumnuclear region, we study a spatial distribution of possible non-circular motions. With this goal we made a map of residuals between the observed velocity field in the $H\alpha$ and the model of the pure circular rotation. The circular model was obtained using the 'tilted-rings' approximation (see previous section) with fixed angles $PA = PA_0$ and $i = i_0$. Fig. 3a shows a 10×10 kpc region of the residual velocity field. This figure reveals a tight correlation between large amplitude of the residuals and spiral arms traced in the $H\alpha$ -isophote. Moreover, large non-circular velocities are detected in the centre ($r = 1 - 5$ arcsec) of the galaxy along its minor axis: $V_{res} = +(20 - 25) \text{ km s}^{-1}$ to NE and $V_{res} = -(40 - 45) \text{ km s}^{-1}$ to SW from the nucleus. Before interpreting these features, let us recall a formula for the projection of velocity vector in the galactic disc after the subtraction of the circular rotation:

$$V_{res} = V_r \sin \varphi \sin i + V_\varphi \cos \varphi \sin i + V_z \cos i, \quad (1)$$

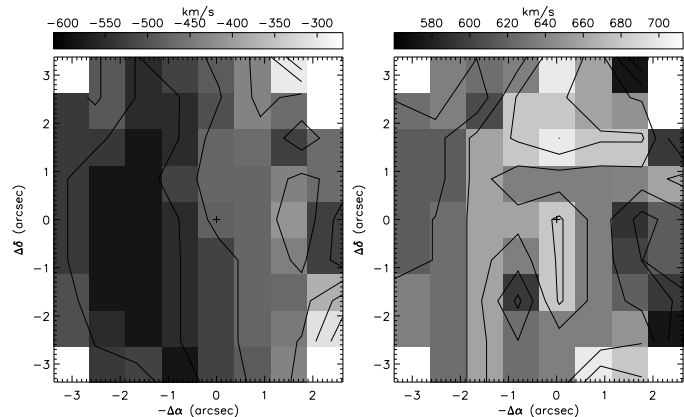


Figure 5. The outflow velocity map (left) and the field of velocity dispersion (right) of the NLR1, where assumptions of two emission regions were applied. The zero-point cross marks to the centre in the continuum images.

where $\{V_r, V_\varphi, V_z\}$ are radial, azimuthal and vertical component of the velocity vector respectively; φ is the azimuthal angle measured from the projected major axis in the plane of the galaxy. Assuming that the motion is only in a galactic plane, then according the first approximation, we have that $V_z \approx 0$. Therefore, in the points which are close to the minor axis ($\varphi \approx 90, 270^\circ$) we observe only a projection of radial motions: $V_{res} \approx V_r \sin i$. The direction of these motions (inflow or outflow) is determined by the orientation of the disc relative to the observer. For Mrk 533 the SW side is closer to the observer (Kinney et al. 2000), that is in accordance with the assumption of trailing spiral arms. In this case, large residual velocities along the minor axis correspond to the outflow motion $40 - 90 \text{ km s}^{-1}$ in an amplitude².

Using this formalism we created a map of inflow/outflow radial streaming motions (Fig. 3b). On this map we avoid points $|\varphi| < 45^\circ$ that form with the major axis. Here the projection of the azimuthal component of residual velocities can be larger than radial ones (for this points should be $|\sin \varphi| < |\cos \varphi|$ because in spiral galaxies V_r and V_φ have same amplitude, see direct measurements by Fridman et al. (2001a, b). Also we show in Fig. 3b the position of the bar (with orientation and axis ratio is in accordance with the NIR photometry reported by Hunt et al. 1997) and spiral arms (see Verdes-Montenegro et al. (1997), their Fig. 6b). The map of radial motions shows complex structures: the outflow in the centre ($r < 5$ arcsec), the gas inflow along the Northern arm at $r = 5 - 15$ arcsec and an outflow again at $r > 15$ arcsec (8.5 kpc) along the Southern spiral arm. The difference in radial motions for the different arms can be a result of their asymmetrical shapes caused by an interaction with other members of the compact group of galaxies. Also the possible position of a co-rotation at $r \approx 15$ arcsec may produce these changes of radial motions in the direction along the spiral arm.

² This speed should decrease if the direction of the outflow lies out of the galactic plane, i.e. $V_z \neq 0$

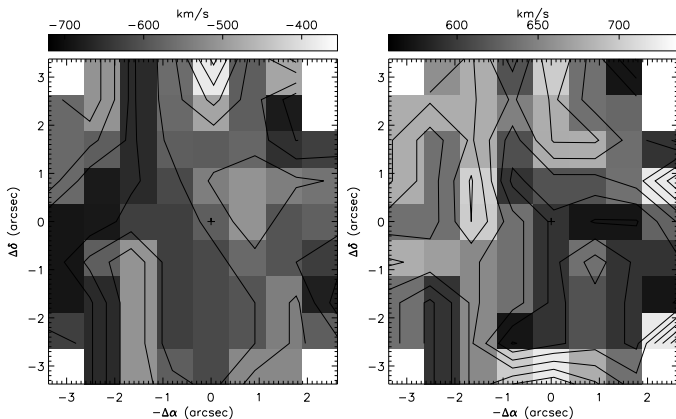


Figure 6. The outflow velocity map (left) and the field of velocity dispersion (right) of the NLR1, where assumption of three emission regions was applied.

4 THE NLR KINEMATICS

In order to investigate the NLR kinematics, in this section we present the analysis of the [OIII] emission line profiles obtained from MPFS data. The shapes of the narrow spectral lines have a blue asymmetry only in the nuclear part (see Fig. 4) of the galaxy. By inspecting the line profiles, the asymmetry can be seen in the $H\alpha$, $H\beta$ and [OIII] lines, and the shapes of the blue part of the lines differ from the various parts of the nucleus emitting region (Fig. 4). Here we have high spectral resolution spectra only for the $H\beta$ + [OIII] lines, observed in 2005, but the $H\beta$ line is significantly weaker than the [OIII] lines and asymmetry is not enough pronounced. Consequently we analyze in more details only the spectra of the [OIII] lines.

It is important to note that we could spatially resolve the region with a blue-wing asymmetry of line profiles. In order to check this, we created a map showing the distribution of brightness of the flux in the broad wing of the [OIII] lines. Indeed, our analysis showed that the FWHM of the spatial distribution was about 2-2.4 arcsec that is significantly larger than the size of the image of the star (seeing was 1.3 arcsec) observed with MPFS directly before the galaxy.

4.1 Line profile analysis

To analyze the shape of the [OIII] lines one can fit the line profiles assuming different functions (Lorentz, Voigt, Gaussian profiles). But taking into account that the line profiles in the emitting region is caused by a motion of the emitters, here we fitted each line with the sum of Gaussian components. We applied a χ^2 minimalization routine in order to obtain the best-fitting parameters. We also assumed that the narrow emission lines can be represented by a sum of Gaussian components. In the fitting procedure, we looked for the minimum number of Gaussian components needed to fit the lines. To limit the number of free parameters in the fit we set some a priori constraints (Popović et al. 2004):

(i) Two Gaussian (e.g. broad and narrow components shown in Fig. 5) representing the [OIII] $\lambda\lambda$ 4959,5007 lines are fixed at the same red-shift and the Gaussian widths are

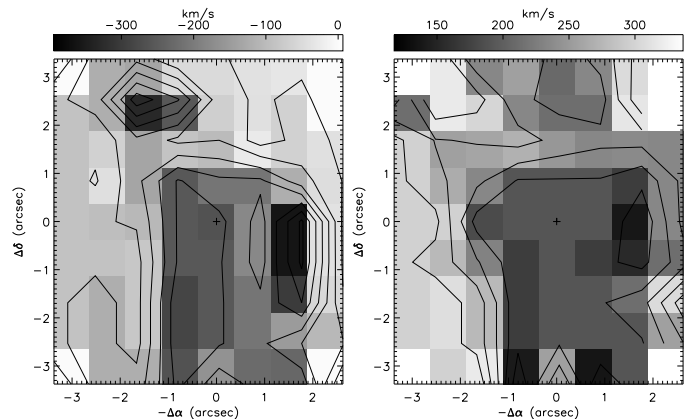


Figure 7. The outflow velocity map (left) and the field of velocity dispersion (right) of the NLR1a.

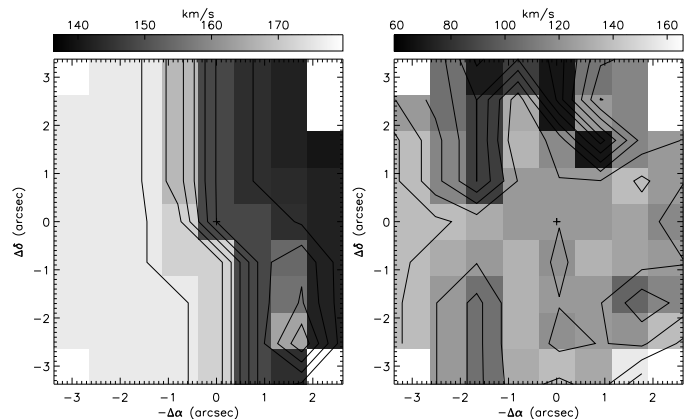


Figure 8. The field of velocity dispersion of the NLR2: 1. The case of fitting spectra with two Gaussians (left); 2. For the case of fitting spectra with three Gaussians (right).

set proportional to their wavelengths,

$$\frac{W_{4959}}{4959} = \frac{W_{5007}}{5007}$$

(ii) We assumed that the intensity ratio of the two [OIII] $\lambda\lambda$ 4959,5007 lines is $\approx 1:3$ (Dimitrijević et al. 2007).

Here we will use the velocity dispersion to present the velocity field ($\sigma = (W/\sqrt{2}) \cdot (c/\lambda)$, where W is the Gaussian width). Outflow velocities are considered to be $V_r = c \times \frac{\Delta\lambda}{\lambda}$, where $\Delta\lambda = \lambda_c - \lambda_b$ is a blue shift, measured between the centre of the narrowest component that is assumed to correspond to the transition wavelength λ_c and those which are blue shifted λ_b (Fig. 4)

As mentioned above (see in Fig. 4) the [OIII] lines show a blue asymmetry, and can be properly fitted with two Gaussian components (Fig. 4b). Moreover, a slightly better fit (concerning χ^2) can be obtained by fitting with three Gaussians (Fig 4c). Therefore, here we will consider the complex [OIII] line region as composed from two or three separated emission regions. When we assume the emission of two regions, we denote those regions as the NLR1 (blue shifted

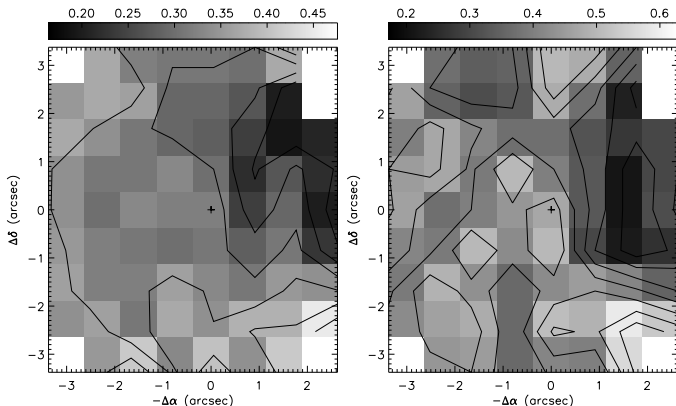


Figure 9. Flux ratio between NLR1 and NLR2 emission components where two (left) and three (right) emission regions are assumed.

component) and NLR2 (non-shifted component). In the case where we assume that the emission is coming from three regions, we additionally consider a NLR1a existence (also the blue-shifted component) region that corresponds to a component placed between the central and broad blue shifted one (Fig. 4c). We started to fit each spectra obtained from spatial MPFS elements, but out of the nucleus (around 8×9 elements) it is not possible to see the asymmetry, so the method of fitting analysis has been applied only in the small frame elements that corresponds to a small region on the sky around 6×7 arcsec.

The velocity maps that we obtained from our analysis are presented in Fig. 5-8. Also we found a map of flux ratios of NLR1 and NLR2, i.e. $\frac{F_{NLR1}}{F_{NLR2}}$ (Fig. 9).

4.2 Assumption of two emitting regions

Assuming the presence of two kinematically separated regions, we fitted the [OIII] lines with two Gaussians (Fig. 4b). As one can see in Fig. 4b the line shapes can be well fitted with two Gaussians, but a small shoulder in the blue part can not be fitted properly with this assumption. The map of the outflow in the NLR1 is presented in Fig. 5 left. As can be seen in this figure, the maximum outflow velocity ($\sim -550 \text{ km s}^{-1}$) is located to the east from the continuum centre (presented as a cross in Fig. 5). A gradient in outflow velocities from the east to the west is present. The obtained difference amongst velocities (from the east to the west) is $\sim 300 \text{ km s}^{-1}$. This supports the idea about the existence of an approaching jet from the active galactic nucleus (Momjian et al. 2003). The velocity field of the outflow has a south-north elongated structure (Fig. 5a), which might be due to the projection of the jet. On the other hand the velocity dispersion field has a relatively small difference in NLR1 ($\sim 560\text{-}670 \text{ km s}^{-1}$), showing a relatively flat velocity field. The intensity ratios in the central part of NLR1/NLR2 are present in Fig. 9 (left). The maximal intensity of the NLR1 is around the optical centre.

The NLR2 velocity dispersion map shows also stratification, where velocity dispersion has values ranging from 150 km s^{-1} to 170 km s^{-1} , having a gradient from the west to the east (Fig. 8 left). This gradient in velocity dispersion has

a possible connection with the radio jet which is also elongated in the same direction (see Section 5). However this should be taken with caution, since the differences in velocity dispersion are too small (around 20 km s^{-1} , that is very close to the range of the error bars of the fitting method).

4.3 Assumption of three emitting regions

As was mentioned above, a slightly better fit can be obtained when we perform a three Gaussian fitting procedure. Moreover, there is an anticorrelation between the outflow velocity map of the NLR1 and dispersion velocity map of NLR2 (see Figs. 5 and 8) that may be caused by fitting the observed profile with an insufficient number of components (only two components). Therefore, we assume that in the nucleus of Mrk 533 three, kinematically separated, emission regions are present on the line-of-sight. The velocity maps of the NLR1 and NLR1a are presented in Figs. 6 and 7. As one can see in Fig. 6 the outflow and velocity dispersion in NLR1 are slightly higher then in the case of two region approximation. The maximum outflow velocities ($\sim -700 \text{ km s}^{-1}$) are located to the east of the optical centre, having a south to north elongated structure. In comparison to the two region approximation, the three region approximation shows that the outflow structure is more complex then the one obtained from two Gaussian fit. Also, the map of velocity dispersion shows several regions around the optical centre with higher velocities (Fig. 6, right). But this should be taken with caution, since the difference in velocity dispersion is small ($\sim 100 \text{ km s}^{-1}$) and the velocity dispersion field of the nucleus of Mrk 533 tends to have a flat distribution, as it was the case in the two Gaussian assumption.

The NLR1a region shows a complex structure around the optical centre, with maximum outflow velocity around -250 to -300 km s^{-1} , and minimum velocity dispersion around $140 - 320 \text{ km s}^{-1}$, see Fig. 7. Also, the ratio between NLR1 and NLR2 fluxes (Fig. 9) indicates a clumpy NLR.

In this case the NLR2 velocity dispersion region is similar to the one in two Gaussian case, where velocity dispersion has values ranging from 70 km s^{-1} to 160 km s^{-1} (Fig 8). As one can see there are some structures which might indicate also a clumpy NLR2.

4.4 The complex NLR: Two or three emitting regions?

Based on our analysis the [OIII] line shapes across the central part of Mrk 533, it can easily be noted that there is an outflow. The outflow also can have a complex structure in velocity and spatial domain. Although the [OIII] line profiles can be well fitted with the assumption of two emitting region (where one is characterized by the presence of an outflow), the better fit of the line shapes can be reached with the three emitting region assumption. Moreover, the anticorrelation between the NLR1 outflow velocity map and the NLR2 velocity dispersion map in the two emission region indicates that there are probably two regions with outflows. Here the outflow velocities range from -500 to -700 km s^{-1} in one region and range from -200 to -400 km s^{-1} in the another. The obtained velocities are in accordance with the outflows registered from the O VI absorption lines, where the

measured velocity of the outflows are -800 and -300 km s^{-1} (Shastri et al. 2006). It seems that these regions in outflow also absorb in the UV radiation. On the other hand, our research of the circumnuclear region (see Section 3) shows that near the nucleus $r < 5$ arcsec there is an outflow, but with a smaller outflow velocity (from -40 to -90 km s^{-1}). This type of outflow was observed only in the narrow component of the $\text{H}\alpha$ profile when the circular rotation velocities were taken into account.

5 CONNECTION BETWEEN THE RADIO, UV AND OPTICAL OUTFLOW

In this part we compare our results obtained in the optical range with the previous results which were obtained in the UV and radio band in order to connect the outflow(s) seen in the NLR1 with the radio jets. An indication of a jet-cloud interaction is the ratio of the emission lines (which can originate from shocks), therefore we first explore the nature of the gas ionization source in the nuclear and circumnuclear region as well as in the spiral structure.

5.1 The source of ionization

In order to identify the nature of the gas ionization source in Mrk 533 we constructed diagnostic diagrams using the emission line intensity ratios, i.e. in Fig. 10 we present $[\text{OIII}]/\text{H}\beta$ vs. $[\text{NII}]/\text{H}\alpha$. According to Veilleux & Osterbrock (1987) we separated the regions corresponding to the ionization by AGN, young OB-stars (HII regions) and shock waves (LINERS) into presented diagram. As a result of short analysis of the spectra, we were able to separate several emitting regions (see Fig. 10, right). Mainly there are three emission regions in the stellar disc plus an emitting region that corresponds to the nucleus. The analysis of the flux ratio of $[\text{OIII}]/\text{H}\beta$ vs. $[\text{NII}]/\text{H}\alpha$ lines shows that spectra belonging to the nucleus (crosses) are located in the part where the ionization of AGN is expected. On the other hand, spectra from the spiral-like emission structure (regions 1, 2 and 3) are mainly located in the HII part of the diagram, i.e. the ionization from hot young stars is present. Note that some points from the region 2, that is closest to the AGN, are located also in the AGN part of the diagram. It means that non-thermal ionization predominates in some parts of the region 2. It is interesting that some points from region 3 are located near the HII/LINER borderline. This may indicate that besides the star bursts ionization, gas may be compressed and that in parts of this region, a shock ionization occurs.

From the inspection of Fig. 10 it is evident that different ionization mechanisms may dominate on different scales. We find that in nucleus part as well as in the regions (1 and 2) which are close to the nucleus the dominant ionization mechanism is AGN-photoionization. However, as we move further away from the nucleus ($\sim \text{kpc}$), jet-cloud interactions may become the main ionization mechanism. In order to discuss the possibility of the dominance of a jet-cloud interaction in some emission regions of Mrk 533, let us recall results obtained by Dopita & Sutherland (1995). They investigated the line fluxes expected from fast, radiative shocks propagating through typical narrow-line AGN clouds. Here, the key parameters controlling the emission-line ratios are shock

velocity and the magnetic parameter. Dopita & Sutherland (1995) found that inclusion of 'precursor' ionization caused by hard radiation generated in the wake of the post-shock, cooling plasma that diffuses outwards, is crucial for explaining differences found in Seyfert and LINER galaxies. It is interesting that faster shocks are required ($\sim 300 - 500 \text{ km s}^{-1}$), that is well fitting our obtained outflow velocities in the NLR1 and NLR1a. We present in Fig. 10 with full circles the predicted line ratios for different shock velocities ('shock plus precursor', see Dopita & Sutherland (1995)). The observed $[\text{OIII}]/\text{H}\beta$ vs. $[\text{NII}]/\text{H}\alpha$ ratios in the nucleus region are consistent with a 'shock plus precursor' model that has shock velocity exceeding 300 km s^{-1} at least, and a magnetic parameter typical for the interstellar medium (Dopita & Sutherland 1995). Moreover, some points from the other three emission regions shown in Fig. 10b are also consistent with a 'shock plus precursor' model, but with smaller velocities $\sim 200 \text{ km s}^{-1}$. Note here that the flux ratios of $[\text{OIII}]/\text{H}\beta$ and $[\text{NII}]/\text{H}\alpha$ are constructed only using narrow lines observed with the MPFS.

5.2 Outflows in the radio, optical and UV emission

To reconstruct the picture obtained from the analysis of the NLR and circumnuclear kinematics we draw Fig. 11, where the outflow velocities in all three components are given. The velocities are measured along the dashed line shown in Fig. 12. The circles in Fig. 11 represent the measured velocity of the outflows from O VI absorption lines (-800 and -300 km s^{-1} , see Shastri et al. 2006). As it can be seen in Fig. 11, there is a stratification in the line-of-sight velocities, that may also indicate a different distribution of these components, as well as, heaving in mind the different absorption densities of the UV. The spatial structure of the outflow is slightly resolved: the high-velocities of ($V_{outflow} > 100 \text{ km s}^{-1}$) NLR1 extends up to 1.5 kpc , and the low-velocity ($V_{outflow} = -(20 - 80) \text{ km s}^{-1}$) emission regions extend up to 2.5 kpc (see Fig. 11). We remind that our spatial resolutions were about 0.7 kpc (1.3 arcsec) on MPFS and 1.4 kpc (2.5 arcsec) with FPI. Since the emission originates far away from the nucleus, one can consider the possibility that the mechanism for the optical line emission may actually be a shock wave, created in a wind (or jet) from the AGN, that is also in accordance with the analysis of the source of ionization (see Section 3.4).

Note here, that with the MPFS and FPI we have detected essentially different components of the outflow. In the first case the multicomponent fitting of the emission lines profiles was carried out and the high-velocity component in the blue wing of the emission lines profiles was studied. In the second case, the narrow spectral range of the FPI did not allow us to analyze the shape of the spectral profile. However, higher (in comparison with MPFS) spectral resolution gives the most accurate measurements of the velocities of the emission line core. Moreover, using a large field of view and better spatial sampling we can determine the differences between the observed velocities and the circular rotation model. Therefore, we can distinguish the peculiar velocities with amplitudes about several tens of km s^{-1} . We illustrated the differences between the MPFS and the FPI measurement on the right side of Fig. 11 where components

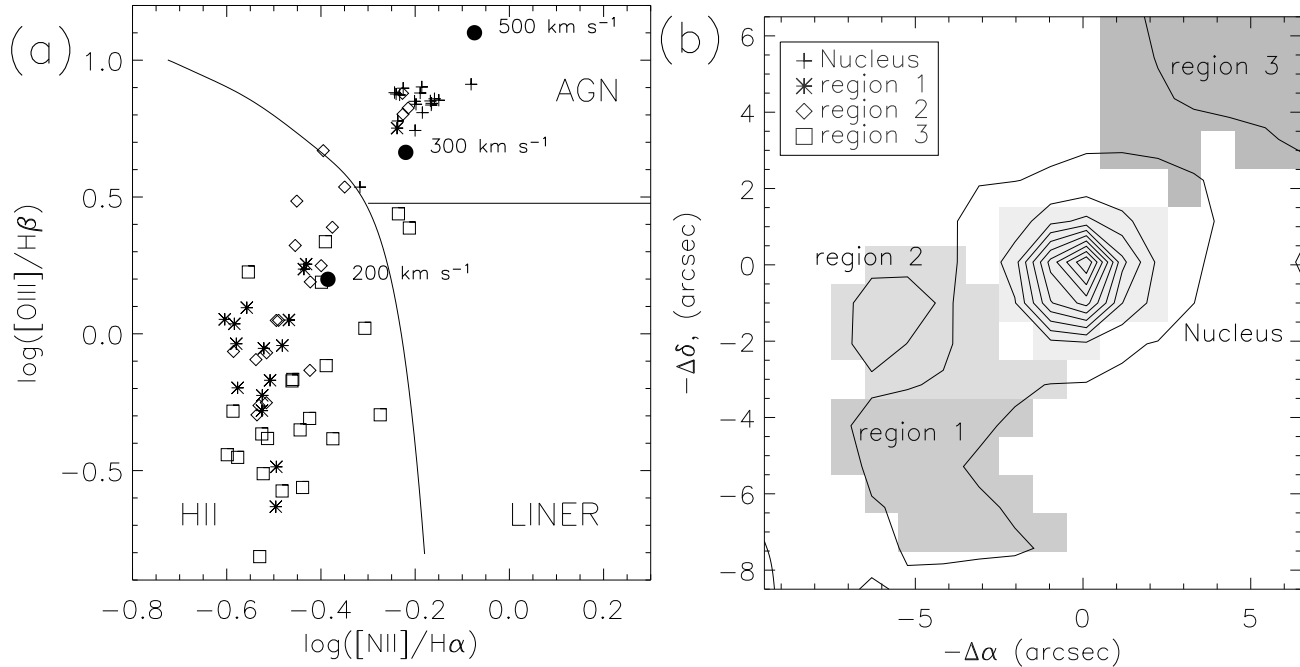


Figure 10. The flux ratio of $[\text{OIII}]/\text{H}\beta$ lines vs. $[\text{NII}]/\text{H}\alpha$ (a) and the map of Mrk 533 with regions for which this ratios are found (b). The $\text{H}\alpha$ isophotes are overlapped on this map. The full circles in Fig. 4a represent the calculated ratio by Dopita & Sutherland (1995), where ‘shock plus precursor’ model were used. The calculated values are for the shock velocities of 200 km s^{-1} , 300 km s^{-1} , and 500 km s^{-1} (the values are given near the full circles).

of the emission lines correspond to the given outflow velocities shown schematically.

To find any connection between the optical and the radio outflow (reported in Unger et al. (1988), Momjian et al. (2003), Middelberg et al. 2004) we draw a map with the optical and radio outflow structures (see Fig. 12). It is indicative to see that the orientation of two jets from two points such as radio sources, are directed to the optical outflow structures. Also, as one can see in Fig. 12, the maximal outflow velocities correspond to the side where the most intensive part of the radio structure is located. Concerning the map shown in Fig. 12, one can speculate that the optical outflow is following the radio one, i.e. that the jet emits in the radio domain, as it is close to the central engine ($r < 1$ arcsec or 0.5 kpc), and farther from the centre of the UV absorption/emission (see Fig. 11) and optical emission occurs ($r = 2 - 4$ arcsec or $1 - 2 \text{ kpc}$). We outline that this optical emission, partly triggered by the shock waves originates from the jet intrusion in to the gaseous ambient medium.

The presence of high-velocity clouds, located close to the passage of the radio jet and centred near the centre of the nucleus, shows that the effects of jet-induced shocks are still important in the nuclear regions. Moreover, the velocity dispersion of the $[\text{OIII}]$ component in the NLR1 is high: ranging from 570 to 720 km s^{-1} . Increased linewidths are expected following turbulent motions of an interaction (e.g. by jet-cloud interaction), but not in passive photoionization by the AGN (see e.g. Clark et al. (1997); Gandhi et al. (2006)). On the other side in both approximation (two and three emission line region) we noted outflows with a relatively high velocity. Therefore, the assumption that the projected radio jets (see Fig. 12) have an influence on NLR1 physics and kinematics seems to be real.

6 CONCLUSION

In this paper we analyzed the spectroscopic observations of Mrk 533 performed by the 6-m telescope of SAO RAS. We investigate the gas kinematics in the spiral and circumnuclear structures. Based on this investigation we are able to conclude the following:

i) We found the parameters of the galactic gaseous disc orientation: $i_0 = (33 \pm 5)^\circ$ and $PA_0 = (306 \pm 4)^\circ$. The parameters are in accordance with the ones obtained by Verdes-Montenegro et al. (1997), but they are significantly different from the ones measured by Amram et al. (2003).

ii) Our analysis of the large-scale ionized gas velocity field shows presence of significant non-circular motions. Also we indicate the outer warping gaseous disc, probably caused by an interaction with the companions. The disc warping was found to be around $13 - 15^\circ$ at distances $r > 20 \text{ kpc}$ (at least in the NW side of the disc).

iii) We created a map of radial motions in the gaseous disc. It shows a very complex non-circular gas motion in Mrk 533, that may be triggered by an interaction. So, the gas inflow along the Northern arm ($5'' < r < 15''$) and streaming motions along the bar were found by analyzing of this map and as well as radial dependence of the dynamical axis PA . A co-rotation at $r \approx 8.5 \text{ kpc}$ may produce changing of radial motions direction along the Northern spiral arms at $r > 15$ arcsec. The circumnuclear outflow in $r < 5$ arcsec along the minor galactic axis was also detected.

iv) The central emitting region of Mrk 533 is complex and can be divided into: the emission of the Sy 2 nucleus (in the very central part) and the star-forming regions which follow the spiral structure of the galaxy. The emission line

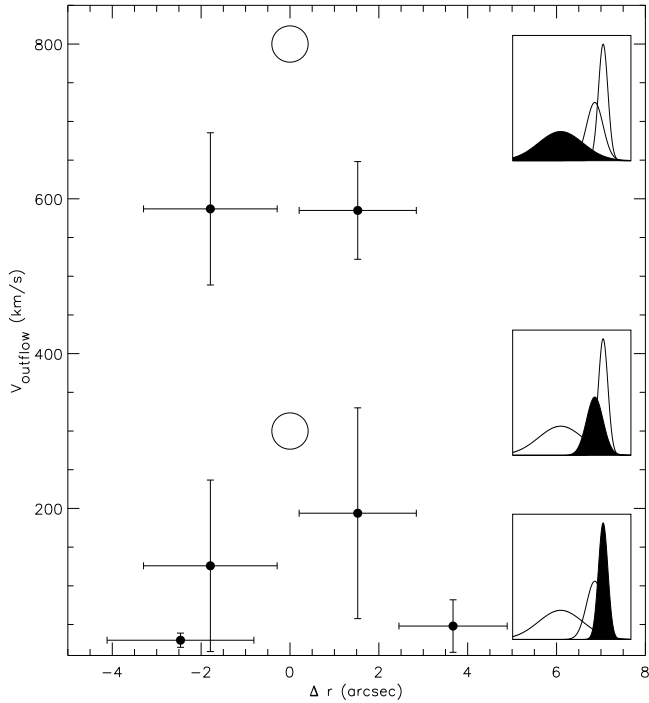


Figure 11. The outflow velocities in the central part of Mrk 533 (within $-4.5'' < r < 5''$) obtained from Gaussian fits of the [OIII] lines (nuclear region) and from the analysis of circumnuclear kinematics of H α (full circles, crosses indicate the interval of scattering $V_{outflow}$ and r). The circles represent the outflow velocities from absorption components in O VI lines (Shastri et al. 2006). The diagrams on the right show a component of the emission profile (marked as black Gaussian) corresponded to the different scales of $V_{outflow}$.

shapes in the region of the nucleus have a blue asymmetry this indicates an outflow from the centre.

To investigate the velocity structures of the nucleus, we assumed that the NLR of Mrk 533 is composed of: (a) two and (b) three kinematically separated regions. From this analysis we can conclude that:

- The [OIII] $\lambda\lambda 4959, 5007$ lines originate from at least two kinematically separated regions: NLR1 contributes to the blue part of the spectral lines, where a gaseous outflow with velocities from -300 km s^{-1} (5 arcsec far from the centre) to -600 km s^{-1} around the nucleus (the velocity dispersion is around $560 - 670 \text{ km s}^{-1}$) exist; NLR2 has a smaller velocity dispersion ($\sim 150 \text{ km s}^{-1}$).

- The complex [OIII] lines may be produced in three kinematically separated regions: NLR1 contributes to the blue part of the spectral lines, with a gaseous outflow with velocities ranging from -500 to -700 km s^{-1} ; the NLR1a with outflow velocities from -350 to -100 km s^{-1} and NLR2 without a significant outflow.

Finally, we can conclude that a stratification in the NLR of Mrk 533 exists, and that it has a range of outflow velocity from $20-50 \text{ km s}^{-1}$ to $600-700 \text{ km s}^{-1}$ on radial distances ~ 2.5 and $\sim 1.5 \text{ kpc}$ accordingly. The structure of the optical outflow seems to be complex, but it seems that the registered outflow(s) in the optical corresponds to the one(s) registered in the UV. Moreover, it is likely that the outflow obtained from the optical emission lines ([OIII] and H α) fol-

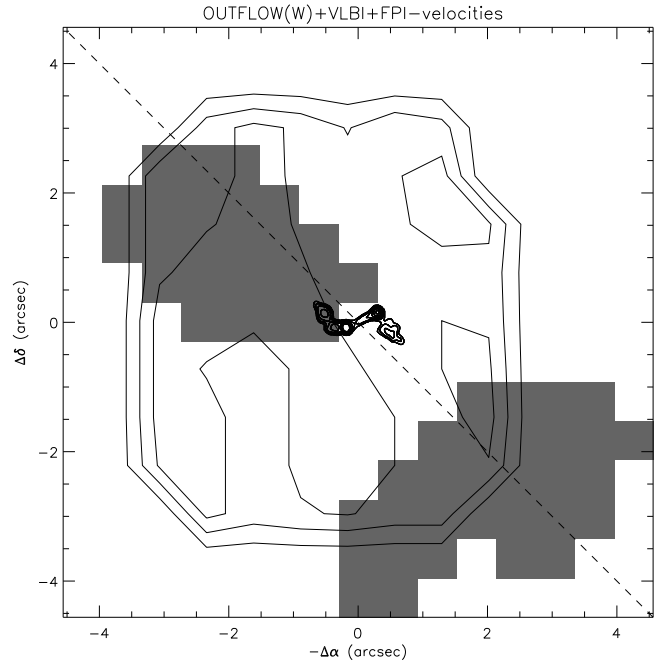


Figure 12. The optical vs. radio outflow: Gray colors shows the position of circumnuclear outflow region seen on Fig. 3b. The iso-lines show the outflow mapped using the [OIII] lines (Fig. 6, left) and feature in the centre is the map of the radio continuum given by (Momjian et al. 2003). The dashed line marks the direction of the x-axis on Fig. 11

lows the radio one and that the complex structure of the optical outflow is generated by the radio jet.

ACKNOWLEDGMENTS

This work is based on observations carried out at the 6-m telescope of the Special Astrophysical Observatory of the Russian Academy of Sciences, operated under the financial support of the Science Department of Russia (registration number 01-43). This research has made use of the NASA/IPAC Extragalactic Database (NED) which is operated by the Jet Propulsion Laboratory, California Institute of Technology, having contract with the National Aeronautics and Space Administration. This work was partly supported by the Russian Foundation for Basic Research (project nos. 06-02-16825). AAS also thanks the Russian Science Support Foundation. This work is a part of the project (146002) ‘Astrophysical Spectroscopy of Extragalactic Objects’, supported by the Ministry of Science of Serbia. We would like to thank to the anonymous referee for very useful suggestions which helped us improve the paper.

REFERENCES

- Afanasiev V. L., Dodonov S. N., Moiseev A. V., 2001, in Ossipkov L. L., Nikiforov I. I., eds, Proc. Int. Conf. Stellar Dynamics: from Classic to Modern, Sobolev Astron. Inst. St Petersburg, p. 103

- Afanasiev V. L., Kostiuk I. P., 1996, in Buta R., Crocer D. A., Elmegreen B. G., et al., eds, Barred galaxies, San Francisco: ASP Conf. Series, 91, p. 233
- Afanasiev V. L., Lipovetskii V. A., Markaryan B. E., Stepanyan Dzh. A., 1980, *Astrofizika*, 16, 193
- Amram P., Plana H., Mendes de Oliveira C., Balkowski C., Boulesteix J., 2003, *A&A*, 402, 865
- Binney J., 1992, *ARA&A*, 30, 51
- Begeman K. G., 1989, *A&A*, 223, 47
- Clark N. E., Tadhunter C. N., Morganti R., Killeen N. E. B., Fosbury R. A. E., Hook R. N., Siebert J., Shaw M. A., 1997, *MNRAS*, 286, 558
- De Robertis M. M., Shaw R. A., 1990, *ApJ*, 348, 421
- Dimitrijević M. S., Popović L. Č., Kovačević J., Dačić M., Ilić D., 2007, *MNRAS*, 374, 1181
- Dopita M. A., Sutherland R. S., 1995, *ApJ*, 455, 468
- Fridman A. M., Khoruzhii O. V., Lyakhovich V. V., Sil'chenko O. K., Zasov A. V., Afanasiev V. L., Dodonov S. N., Boulesteix J., 2001a, *A&A*, 371, 538
- Fridman A. M. et al., 2001b, *MNRAS*, 323, 651
- Hickson P., 1982, *ApJ* 255, 382
- Gandhi P., Fabian A. C., Crawford C. S., 2006, *MNRAS*, 369, 1566
- Hunt L. K., Malkan M. A., Rush B., Bica M. D., Nelson B. O., Stanga R. M., Webb W., 1997, *ApJS*, 108, 229
- Iono D., Yun M. S., Mihos J. C., 2004, *ApJ*, 616, 199
- Kinney A. L., Schmitt H. R., Clarke C. J., Pringle J. E., Ulvestad J. S., Antonucci R. R. J., 2000, *ApJ*, 537, 152
- Laurikainen E., Moles M., 1988, *AJ*, 96, 470
- Miller J. S., Goodrich R. W. 1990, *ApJ*, 355, 456
- Moiseev A. V., 2002, *Bull. Spec. Astrophys. Obs.*, 54, 74 (astro-ph/0211104)
- Moiseev A.V., Valdés J.R., Chavushyan V.H., 2004, *A&A*, 421, 433 26, 665
- Middelberg E. et al., 2004, *A&A* 417, 925
- Momjian E., Romney J. D., Carilli C. L., Troland T. H., 2003, *ApJ*, 597, 809
- Perez M. J., Tissera P. B., Lambas D. G., Scannapieco C., 2006, *A&A*, 449, 23
- Popović L. Č., Mediavilla E., Bon E., Ilić D., 2004, *A&A*, 423, 909
- Schmitt H., Fernandes R., Delgado R., Storchi-Bergmann T., Martins L., Heckman T., 2003, *ApJS*, 148, 327.
- Shastri P., Murthy J., Hutchings J., Wills B. J., 2006, *ApJ*, 646, 76
- Shuder J. M., Osterbrock D. E., 1981, *ApJ*, 250, 55
- Tran H. D., 1995, *ApJ*, 440, 578
- Unger S. W. et al. 1988, *MNRAS*, 234, 745
- Verdes-Montenegro L., del Olmo A., Perea J., Athanasoulas E., Marquez I., Augarde R., 1997, *A&A* 321, 409
- Veilleux S., 1991, *ApJ*, 369, 331
- Veilleux S., Osterbrock D. M., 1987, *ApJS*, 63, 295
- Vogel N. S., Rand R. J., Gruendl R. A., Teuben P. J., 1993, *PASP*, 105, 666